Topological valley plasmons in twisted monolayer-bilayer graphene moiré superlattices

Weiwei Luo,[1,2,*] Jiang Fan,[1] Alexey B. Kuzmenko,[3] Wei Cai,[1] and Jingjun Xu[1]

[1]*The Key Laboratory of Weak-Light Nonlinear Photonics, Ministry of Education, School of Physics and TEDA Applied Physics Institute, Nankai University, Tianjin 300457, China*

[2]*Collaborative Innovation Center of Extreme Optics, Shanxi University, Taiyuan, Shanxi 030006, China*

[3]*Department of Quantum Matter Physics, University of Geneva, 1211 Geneva, Switzerland*

(Received 12 October 2023; revised 2 May 2024; accepted 26 June 2024; published 8 July 2024)

In topological photonics, artificial photonic structures are constructed for realizing nontrivial unidirectional propagation of photonic information. On the other hand, moiré superlattices are emerging as an important avenue for engineering quantum materials with novel properties. In this paper, we combine these two aspects and demonstrate theoretically that moiré superlattices of small-angle twisted monolayer-bilayer graphene provide a natural platform for valley-protected plasmons. Particularly, a complete plasmonic bandgap appears stemming from the distinct optical conductivities of the ABA and ABC stacked triangular domains. Moreover, the plasmonic crystals exhibit nonzero valley Chern numbers and unidirectional transport of plasmonic edge states protected from intervalley scattering is presented.

DOI: 10.1103/PhysRevB.110.035408

I. INTRODUCTION

Graphene plasmons, hybrids of Dirac quasiparticles and photons, exhibit low-loss, strong electromagnetic confinement and electrical tunability [1–3]. Graphene plasmons provide excellent opportunities for exploring light-matter interactions at the nanoscale, which is promising for applications in integrated photonics [4] and biosensing [5]. Particularly, constructing graphene plasmonic crystal (GPC) provides an efficient approach for modulating plasmonic band structures [6–8]. By introducing the concept of topology, unidirectional propagation of graphene plasmons protected against disorder and backscattering can be realized [9–11]. Especially, infrared topological graphene plasmons are predicted by breaking time-reversal symmetry with magnetic fields [9,10]. Meanwhile, the valley binary degree of freedom can be utilized by breaking inversion symmetry [12–14], and topologically robust transport of valley-locked graphene plasmons were presented theoretically [11]. However, the requirements of complex artificial geometries and configurations obstruct the experimental realizations of topological graphene plasmons.

On the other hand, by stacking and twisting different layers of van der Waals materials, two-dimensional (2D) moiré superlattices are emerging as an important avenue for engineering quantum materials with novel properties [15–21]. In particular, in small-angle twisted heterostructures, atomic reconstruction effects generate domain walls separating two kinds of periodically arranged domains with different stacking orders [22–24], with the period a that can be flexibly manipulated by varying twist angle θ according to the formula $a = a_0/[2\sin(\theta/2)]$ (a_0 is the lattice constant of individual layer). Specifically, a can reach hundreds of nanometers for twisted graphene layers with $\theta < 0.1^\circ$ [25,26], comparable to the wavelength of graphene plasmons. Consequently, the regular modifications of the electronic structures and optical properties provide a natural and lithography-free host for GPCs, as demonstrated from recent studies on plasmonic crystal response of small-angle twisted bilayer graphene moiré superlattices [25,27]. However, the stacking domains, which dominate most regions of the superlattices hold identical plasmonic responses, and the limited discrepancy near the domain walls does not open a complete plasmonic bandgap.

With the rapid explorations of twisted heterostructures, reconstructed moiré superlattices with two types of stacking domains of different optical responses are emerging [24,26,28–30]. In this paper, the effect of triangular domains with distinct optical conductivities on the plasmonic band structures is revealed. In particular, the plasmon properties of small-angle twisted monolayer-bilayer graphene (tMBG) are investigated, whose moiré superlattices consist of triangular domains with the Bernal (ABA) and the rhombohedral (ABC) stacking [26,31], as illustrated in Fig. 1(a). The ABA and ABC graphene have different electronic band structures [32–34] where the ABA graphene is a semimetal with a tunable band overlap, while the ABC one is a semiconductor with a gate-tunable band gap and a flat band. Therefore, the two stacking show distinct optical conductivities [35,36]. Here we demonstrate theoretically that tMBG moiré superlattice provides a natural platform for GPC, where complete plasmonic bandgap occurs. Specifically, the pronounced tail of interband transitions from the ABC graphene yields sufficient difference between plasmon response of the two stacked domains. Furthermore, the effects of nontrivial chiral valley topology of the GPC are emphasized. Finally, robust transport of graphene plasmon waves with suppressed intervalley scattering is shown at the interfaces separating two GPCs with opposite valley Chern numbers. Our study motivates further

*Contact author: weiwei.luo@nankai.edu.cn

 ©2024 American Physical Society

explorations of photonic phenomena in the rich platform of reconstructed moiré superlattices.

II. PLASMONIC BAND STRUCTURES

A. Optical conductivities of the ABA and ABC stacked graphene

Generally, plasmon wave vector q of graphene is related to its conductivity $\sigma(\omega)$ through

$$q = 2\omega\varepsilon_0\varepsilon_r i/\sigma(\omega), \tag{1}$$

where ω is the light frequency and ε_r is the effective dielectric constant of environment. To reveal plasmon response of the ABA and ABC graphene under doping, their electronic band structures were calculated from the tight-binding model self-consistently [37] and optical conductivities can be obtained from the Kubo formula for the intraband ($\sigma_{\rm D}$) and interband ($\sigma_{\rm IB}$) terms, following the approach adopted in previous studies [35,36,38,39]. Figures 1(b)–1(e) show the representative results for a back-doped carrier density of 2×10^{13} cm^{-2}, which is easily achievable in experiments [40] (see Appendix A for results at other doping levels).

While the Drude terms are similar between the two stacking orders, with the one for the ABA graphene being slightly stronger [36] [Figs. 1(c) and 1(e)], the obtained interband terms $\sigma_{\rm IB}$ are distinct, in agreement with previous reports [35]. For the ABC graphene, the doping induced an electronic bandgap between bands $b1$ and $t1$ [Fig. 1(d)]. Consequently, the two strong transition peaks P1 and P2 in the curve of Re$\sigma_{\rm IB}$ in Fig. 1(e) correspond to transitions from band $t1$ to $t2$ and from band $b1$ to $t2$, respectively, and their energy difference reflects the size of the electronic bandgap [35]. On the other hand, the interband transitions are strongest at P3 for the ABA graphene [Fig. 1(c)] [35,38], which is at around $\sqrt{2}\gamma_1$ and barely moves with doping (γ_1 is the nearest-neighbor interlayer coupling strength in the tight-binding model).

According to Eq. (1), the ratio between real parts of q, i.e., Re(q), of the two stacking can be obtained from $\chi = {\rm Im}\sigma_{\rm ABC}/{\rm Im}\sigma_{\rm ABA}$. Figure 2(a) compares the extracted Imσ within a frequency range between 600 and 1300 cm^{-1}, where tails of the intraband and interband transitions are observed. If only the intraband terms are considered, a constant value of $\chi = \chi_0 = 0.78$ is obtained for all the frequencies, as shown in Fig. 2(b). Actually, the value of χ_0 depends on the Fermi velocities for the two stacking orders, and varies slightly with different doping levels (Appendix A). In reality, the intraband terms dominate the conductivities at lower frequencies, and χ is close to χ_0. With the increase of the light frequency, the intraband terms decrease while the interband terms contribute more. Moreover, the ABC graphene presents lower values of Im$\sigma_{\rm IB}$, stemming from the influence of the intense peak P1 shown in Fig. 1(e). Consequently, χ decreases dramatically with the increase of the light frequency, reaching 0.5 at around $\omega = 1200$ cm^{-1}. Therefore, a big difference of Re(q) between the two stacking graphene can be obtained.

Generally, graphene plasmons are weakly damped if the light frequency is far below the interband transitions and the intraband term dominates [1,2]. Here, to clarify influence of the interband transitions on plasmon damping, the interband damping factor $\kappa_{\rm IB} = {\rm Re}\sigma_{\rm IB}/{\rm Im}\sigma$ [2,3] is studied and compared with the intraband one $\kappa_{\rm D} = {\rm Re}\sigma_{\rm IB}/{\rm Im}\sigma$. As shown in Fig. 2(c), with the increase of the light frequency, $\kappa_{\rm IB}$ increases with the rate faster for the ABC graphene than for the ABA one, stemming from the stronger interband transition of the ABC graphene. Nonetheless, $\kappa_{\rm IB}$ stays at a same level of $\kappa_{\rm D}$ for the considered frequency range if assuming same values of electronic broadening factors in the Kubo formula (Appendix A), which are both 1 meV in this calculation (a value achievable at low temperatures [3]). Therefore, interband transitions related plasmon damping is still quite weak, as the light frequency is well below the interband transition peaks. Similar results can be obtained for other doped carrier densities (Appendix A).

B. Plasmonic band structures and valley topology

Based on the large difference between plasmon response of the ABA and ABC graphene, next we calculate plasmonic band structures of the moiré superlattices. As illustrated in Fig. 2(d), the interlaced triangular lattices of ABA and ABC graphene form a natural photonic crystal for graphene plasmons, with a rhombic unit cell made of two triangular domains. The plane-wave expansion method (PEM) is employed for calculating plasmonic band structures, where an eigenproblem for the electromagnetic potential $\varphi(\mathbf{r})$ is solved (Appendix B). Figure 2(d) presents the plasmonic band structures for superlattice constant $a = 150$ nm. The first plasmonic band has a maximum at the K (K') point, while the second band is lowest at the M point. Particularly, a complete plasmonic bandgap of around 20 cm^{-1} wide is observed at around $\omega = 1270$ cm^{-1}. The evolution of plasmonic band structures with a is shown in Fig. 9 below. Clearly, the opening of plasmonic bandgap stems from the lower value of χ at high frequency. Here, domain walls between the ABA and ABC graphene are ignored for simplicity, and their influence will be discussed later.

Importantly, triangular domains with different optical conductivities break the inversion symmetry, which is the key to valley photonics [11–13]. Therefore, nontrivial topology of the GPC is investigated by calculating the valley Chern numbers $C_\nu = \frac{1}{2\pi i}\int_{\Delta_\nu} d^2\mathbf{k}F(\mathbf{k})$ [11], where ν is the valley index (K or K'), $F(\mathbf{k}) = \nabla_{\mathbf{k}} \times \langle\varphi_{\mathbf{k}}|\nabla_{\mathbf{k}}|\varphi_{\mathbf{k}}\rangle$ is the Berry curvature, $\varphi_{\mathbf{k}}$ is the eigenstate of $\varphi(\mathbf{r})$ at wave vector $\mathbf{k}$, and Δ_ν represents the integral triangle of each valley ν. Figure 2(e) presents the distribution of $F(\mathbf{k})$ for the first plasmonic band. As expected [11,13,14], opposite Berry curvatures are observed for the two valleys, yielding nonzero and opposite valley Chern numbers $C_{\rm K'} = -C_{\rm K} = 0.14$. They are not exactly at one half, which is well noticed in a similar study [41]. Since the bandgaps are largely opened, the Berry curvature for both valleys will overlap with each other, as shown in Fig. 2(e). As a consequence, the valley Chern number is not exactly 0.5. Nonetheless, protection of the topological valley phase is still well ensured [41], as shown below. Besides, the broken inversion symmetry would lift of the degeneracy between the two sublattice pseudospins, and valley chiral states would appear [12,42]. This is confirmed from phase distributions of the z components of electric fields E_z in Fig. 2(f) (calculated using the finite-element method). For the K (K′) valley, the E_z phase increases clockwise (counterclockwise) by 2π at each unit-cell corner. Thus the two valleys have opposite circular

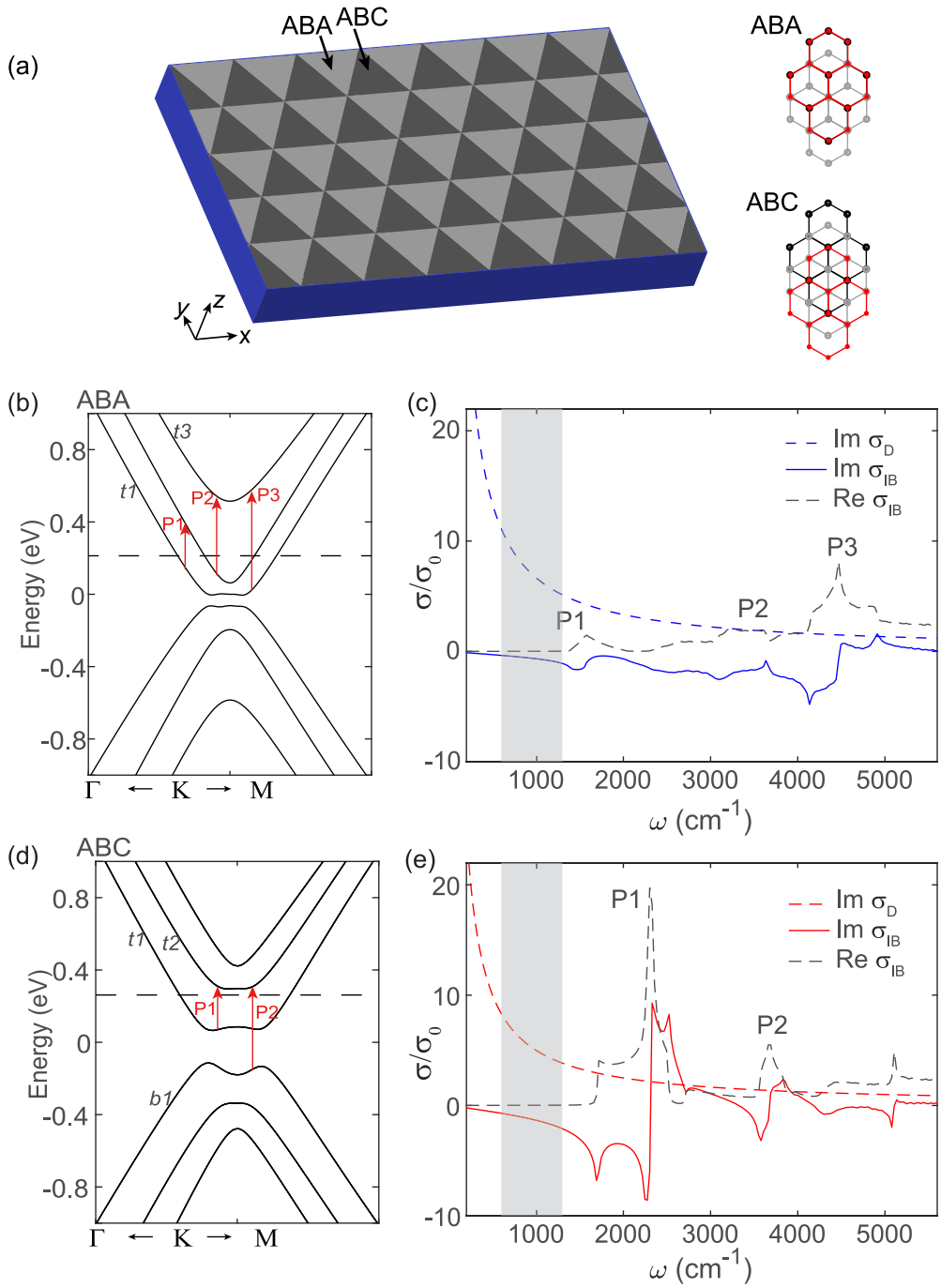

FIG. 1. Moiré superlattices made of twisted monolayer-bilayer graphene. (a) Sketch of a moiré superlattice made of domains of ABA and ABC stacked graphene. The right part represents atomic structures of the two stacking orders, where the symbols with black, gray, and red colors label the first, second, and third atomic layers, respectively. (b) Calculated electronic band structure of the ABA graphene. (c) Frequency dependence of the calculated optical conductivities for the ABA graphene, including imaginary part of the intraband transition term ($\mathrm{Im}\sigma_{\mathrm{D}}$), imaginary ($\mathrm{Im}\sigma_{\mathrm{IB}}$), and real ($\mathrm{Re}\sigma_{\mathrm{IB}}$) parts of the interband transition term. (d), (e) Same as (b) and (c), but for the ABC graphene.

orbital angular momentums (OAMs) [43], and unidirectional excitation of these valley chiral states can be realized by sources carrying OAM with proper chirality [12,43].

III. TOPOLOGICALLY PROTECTED EDGE STATES

Topologically protected edge states can be created at the interface between two graphene plasmonic crystals with opposite valley Chern numbers [11]. As an example, we study the interface structures shown in Fig. 3(a) (see Appendix C for calculation details). The regions GPC1 and GPC2 possess domains of ABA and ABC with reversed orders, and therefore carry opposite valley Chern numbers. As plotted in Fig. 3(b), the edge states cross the plasmonic bandgap, with opposite directions of group velocity near the two valleys. Dispersions of edge states for other geometric parameters

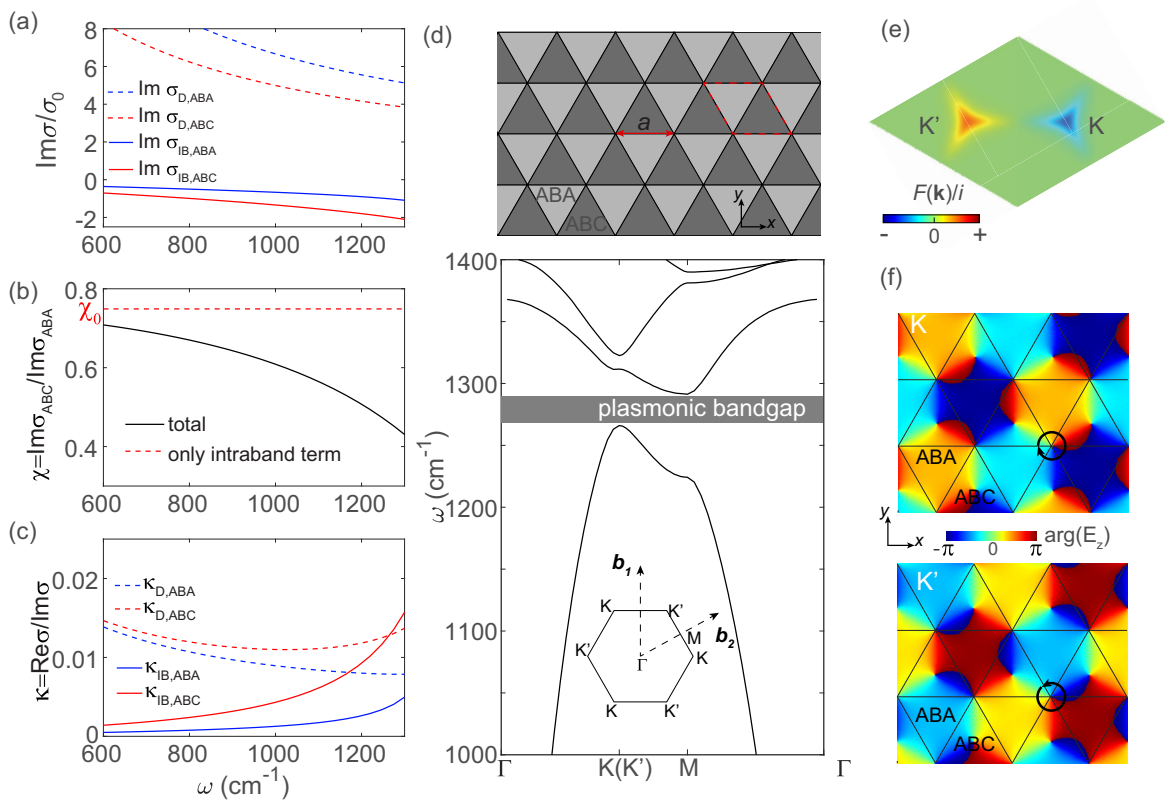

FIG. 2. Plasmonic band structures of the moiré superlattices. (a) Extracted curves of $\mathrm{Im}\sigma_{\mathrm{D}}$ and $\mathrm{Im}\sigma_{\mathrm{IB}}$ for the two stacked graphene within the frequency range marked in Figs. 1(c) and 1(e) (gray regions). (b) Frequency dependence of χ. χ_0 is the value considering only the Drude terms. (c) Plot of intraband (κ_{D}) and interband (κ_{IB}) damping factors for the two stacking orders. (d) (Top) Sketch of the graphene plasmonic crystal made of moiré superlattices. The dashed rhombus labels a unit cell, with lattice constant of a. (Bottom) Calculated plasmonic band structures of the GPC for $a = 150$ nm. The inset shows the Brillouin zone and its reciprocal vectors $\mathbf{b}_1$, $\mathbf{b}_2$. (e) Distributions of the Berry curvature $F(\mathbf{k})$ for the first plasmonic band. (f) Phase distributions of the z components of electric fields for the K and K' valleys at the first band.

are presented in Appendix C. Figure 3(c) exhibits the local electric field confinement near the interface and the opposite directions of energy flux for the two edge states near the K (left) and K' (right) valleys. Moreover, robust propagation of graphene plasmons protected from intervalley scattering are demonstrated at $\omega_0 = 1270\ \mathrm{cm}^{-1}$ in Figs. 3(d)–3(f). As a representative example, a Z-shape waveguide is constructed [Fig. 3(e)] and the propagation of graphene plasmons is compared with the straight one [Fig. 3(d)]. Graphene plasmon waves are excited by a right-hand circularly polarized magnetic point dipole [inset of Fig. 3(e)]. Besides, to model the absorption loss, a weak damping factor value $\kappa = \mathrm{Re}\sigma/\mathrm{Im}\sigma = 1/300$ is assumed for all the graphene nanostructures, which might be achieved at low temperature for encapsulated graphene [3]. For both cases, the excited plasmon waves propagate along the interfaces unidirectionally. Moreover, according to the attenuation of plasmon power plotted in Fig. 3(f), the absorption (analytic curve of slope $\kappa\omega_0/2v_g$, where v_g is the group velocity) is the only source of propagation loss. Strikingly, the plasmon waves can go around the 120° corners without intervalley scattering. Notably, various approaches might be explored to compensate the plasmon loss, for instance, via gain media [44], stimulated electron tunneling [45], nonlinear optical effects [46], and synthesized complex frequency excitation [47].

In practice, fabrications of the periodic moiré superlattices are advancing with the rapid understanding of morphology [22–24,48] and improvements of stacking techniques [49]. Particularly, moiré patterns with tunable periodicity and ultralow disorder have been reported recently [50]. Furthermore, based on the controllable switching and local arrestments of stacking domain orders in tMBG [26], a possible route for preparing the interface structures could be envisioned (Appendix D). Moreover, various strategies can be employed to enlarge the difference of plasmon response between the two domains, like engineering the dielectric environment [51] and exploring the stacking domain-dependent surface functionalization [52], which would increase the plasmonic bandgap and thus minimize the influence of fabrication inaccuracy. Experimentally, the edge states can be excited near a resonant antenna by far-field illumination [7] (Fig. 14 in Appendix D) and detected via the well-demonstrated technique of scattering-type scanning near-field microscopy (s-SNOM).

IV. INFLUENCE OF THE DOMAIN WALLS

Finally, influence of the domain walls is discussed. Various kinds of domain walls between the ABA and ABC graphene can exist [26,53]. Here, for simplicity, we assume identical conductivity profile along the three directions across the

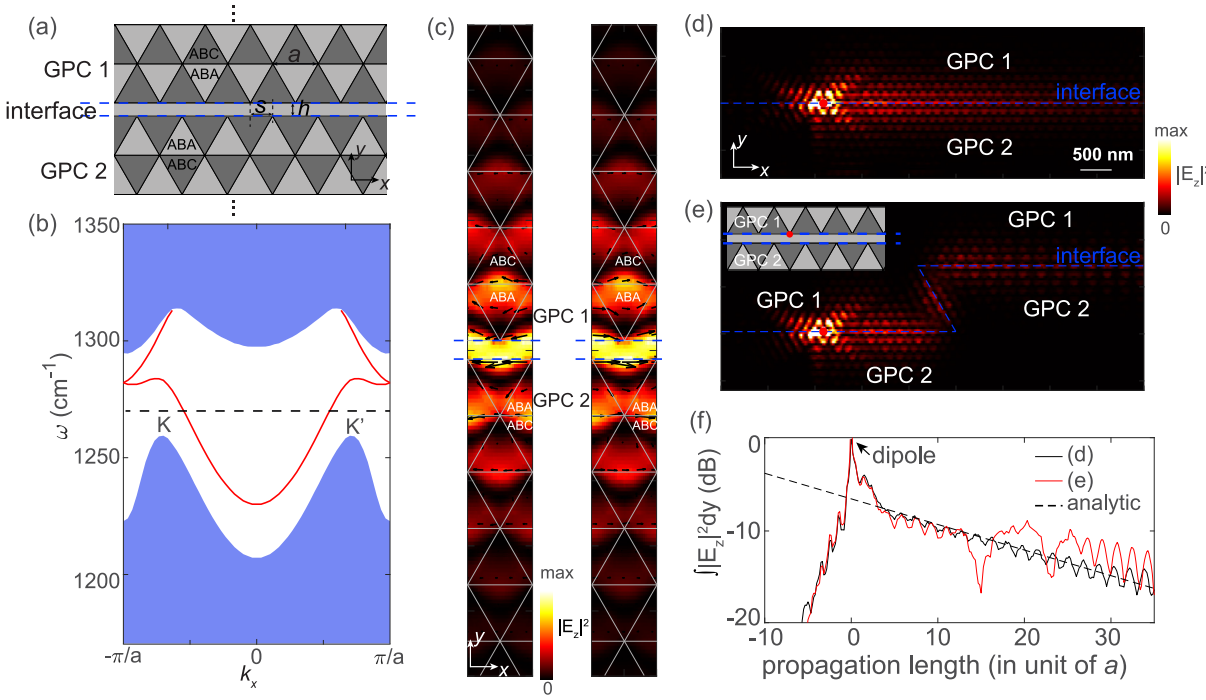

FIG. 3. Valley topologically protected edge states. (a) Sketch of the studied interface structures, where an interface (marked within the blue lines, in x direction) separates two plasmonic crystals (GPC1 and GPC2) with opposite valley Chern numbers. The two GPCs are shifted in x direction by s, and gapped in y direction by h. The interface is assumed as ABA stacked graphene. (b) Dispersion of the edge states (represented by the red curves) for wave vectors in x direction ($k_y = 0$). Here, the geometric parameters are $h = a/(2\sqrt{3})$, and $s = 0.5a$. The blue regions mark the 2D plasmon states. (c) Spatial distributions of $|E_z|^2$ and energy flux at the edge states near the K (left) and K' (right) valleys at $\omega_0 = 1270\ \mathrm{cm}^{-1}$ as labeled in (b) (dashed line). Length and direction of the black arrows represent magnitude and direction of the energy flux, respectively. These values are extracted at 20 nm above graphene. [(d), (e)] Propagation of graphene plasmons along the straight (d) and Z shape (e) interfaces (labeled by blue lines) at the light frequency of $1270\ \mathrm{cm}^{-1}$. The inset in (e) illustrates top view of the point sources (red dots), which sit 10 nm above the graphene surfaces. (f) Propagating length dependence of the plasmon powers calculated by integrating $|E_z|^2$ along the directions perpendicular to the interfaces. The analytic curve (in dashed black) is presented with a slope of $\kappa\omega_0/2v_g$.

domain walls as indicated in Fig. 4(a), and consider two kinds of contributions from the walls. Firstly, instead of a infinite sharp boundary ($\delta = 0$), a transition boundary with finite width $\delta = 6$ nm [26,53] is assumed, which can be described by

$$M(x) = \frac{\sigma_{\mathrm{ABA}} - \sigma_{\mathrm{ABC}}}{2}\mathrm{erf}\left(\frac{x}{\sqrt{2}\delta}\right) + \frac{\sigma_{\mathrm{ABA}} + \sigma_{\mathrm{ABC}}}{2}, \quad (2)$$

where $\mathrm{erf}(x)$ is the error function. Secondly, a peak in the conductivity curve might emerge at the boundary stemming from the distinct electronic band structures like the case of bilayer graphene [54]. This is described by a Gaussian function $g\frac{\sigma_{\mathrm{ABA}}+\sigma_{\mathrm{ABC}}}{2}\exp(\frac{-x^2}{2\delta^2})$ [Fig. 4(b)], where g represents weight of this term. Figure 4(a) plots conductivity profiles for the three cases: infinite sharp boundary ($\delta = 0$), transition boundary with $\delta = 6$ nm, $g = 0$, and transition boundary with $\delta = 6$ nm, $g = 0.2$. The plasmonic band structures for the GPC are recalculated, and presented in Fig. 4(c). As observed, the transition boundaries lower the entire plasmonic bands, while the bandgap width is barely changed. Besides, although the bandgap width is reduced by including the Gaussian term, complete plasmonic bandgap is still observable for the moderate value of $g = 0.2$ (close to the value for domain walls of twisted bilayer graphene in reality [25]).

V. CONCLUSIONS

In conclusion, small-angle tMBG moiré superlattices are demonstrated as natural GPCs with complete plasmonic bandgap. Moreover, the inversion symmetry is broken, and valley topology of the GPC is revealed. Our studies thus provide an avenue for realizing unidirectional propagating of graphene plasmons protected from intervalley scattering. Therefore, various tunable and compact valley plasmonic devices including resonators, modulators, and switches can be foreseen, which are promising for applications in integrated photonics and biosensing. More importantly, our studies demonstrate topological plasmon polariton effects of domains with distinct optical response, which can be generally applied for exploring various kinds of photonic phenomena with the advance of new and complex moiré superlattices [20,55–59], such as topological phonon polaritons [60] in twisted hBN layers [30], topological exciton polaritons [61] in twisted

TABLE I. Values of the coupling parameters, in unit of eV.

γ_0	γ_1	γ_3	γ_4
3.12	0.377	0.29	0.12

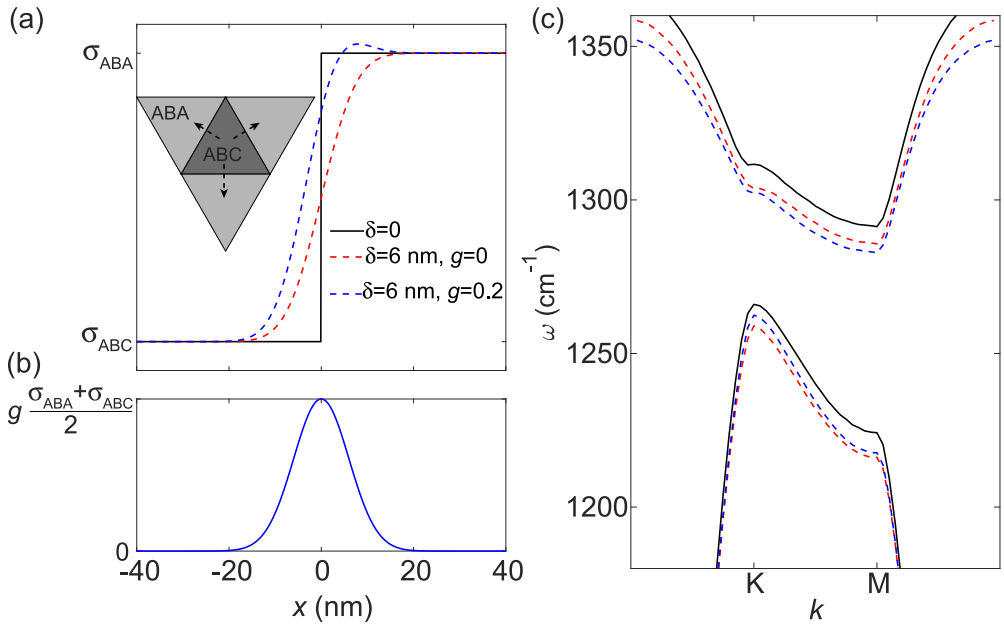

FIG. 4. Influence of the domain walls on plasmonic band structures. (a) Conductivity profiles for the three cases: sharp boundary ($\delta = 0$), transition boundary ($\delta = 6$ nm, $g = 0$), and transition boundary ($\delta = 6$ nm, $g = 0.2$). (b) Profile of the conductivity with a Gaussian distributions, centering at the middle of the boundary. (c) Bulk plasmonic dispersions calculated for the three cases shown in (a).

transition metal dichalcogenide materials [23,29]. Moreover, the plasmon response considered here is mainly contributed by the intraband terms, whereas the interband plasmons [62] can be quite interesting and studied in the future.

ACKNOWLEDGMENTS

This work has been supported by the National Key Research and Development Program of China (Grants No. 2023YFA1407200, No. 2022YFA1404800), the National Natural Science Foundation of China (Grants No. 12004196, No. 12127803, No. 12074200), Guangdong Major Project of Basic and Applied Basic Research (Grant No. 2020B0301030009), Changjiang Scholars and Innovative Research Team in University (IRT13_R29) and the 111 Project (B23045). The work of A.B.K. was supported by the Swiss National Science Foundation.

APPENDIX A: ELECTRONIC BAND STRUCTURE AND CONDUCTIVITY CALCULATIONS

1. Tight-binding model

Tight-binding model is employed for calculating band structures of the ABA and ABC graphene [37,38]. In the basis $|A_1\rangle$, $|B_1\rangle$, $|A_2\rangle$, $|B_2\rangle$, $|A_3\rangle$, $|B_3\rangle$, the Hamiltonian of ABA stacking can be written as

$$H = \begin{pmatrix} -\Delta_{12} & \gamma_0 f & \gamma_1 & -\gamma_4 f^* & 0 & 0 \\ \gamma_0 f^* & -\Delta_{12} & -\gamma_4 f^* & \gamma_3 f & 0 & 0 \\ \gamma_1 & -\gamma_4 f & 0 & \gamma_0 f^* & \gamma_1 & -\gamma_4 f \\ -\gamma_4 f & \gamma_3 f^* & \gamma_0 f & 0 & -\gamma_4 f & \gamma_3 f^* \\ 0 & 0 & \gamma_1 & -\gamma_4 f^* & \Delta_{23} & \gamma_0 f \\ 0 & 0 & -\gamma_4 f^* & \gamma_3 f & \gamma_0 f^* & \Delta_{23} \end{pmatrix}, \tag{A1}$$

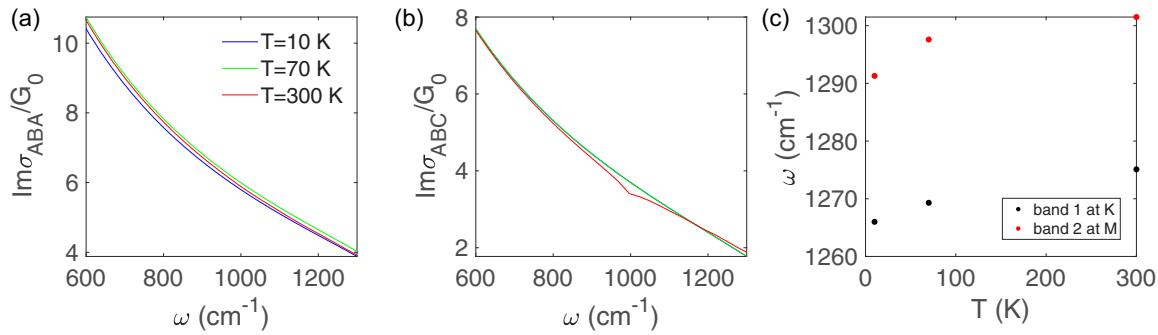

FIG. 5. Calculated temperature dependence of the imaginary parts of optical conductivities for the ABA (a) and ABC (b) graphene, in together with the robustness of the bandgap with temperature (c).

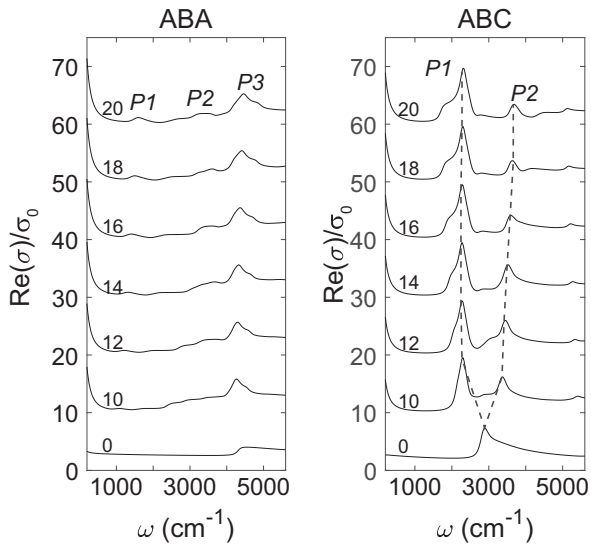

FIG. 6. Real parts of the calculated conductivities for the ABA and ABC graphene at different backside-doped carrier densities n_{back} = 0, 10, 12, 14, 16, 18, and 20 × 10^{12} cm^{-3}. The curves are sequentially shifted by a value of 10 for clarification. Here, electronic broadening parameters are assumed as $\Gamma_{\text{IB}} = \Gamma_{\text{D}} = 10$ meV.

and for the ABC stacking, the Hamiltonian is

$$H = \begin{pmatrix} -\Delta_{12} & \gamma_0 f & \gamma_1 & -\gamma_4 f^* & 0 & 0 \\ \gamma_0 f^* & -\Delta_{12} & -\gamma_4 f^* & \gamma_3 f & 0 & 0 \\ \gamma_1 & -\gamma_4 f & 0 & \gamma_0 f^* & \gamma_3 f & -\gamma_4 f^* \\ -\gamma_4 f & \gamma_3 f^* & \gamma_0 f & 0 & -\gamma_4 f^* & \gamma_1 \\ 0 & 0 & \gamma_3 f^* & -\gamma_4 f & \Delta_{23} & \gamma_0 f \\ 0 & 0 & -\gamma_4 f & \gamma_1 & \gamma_0 f^* & \Delta_{23} \end{pmatrix}. \tag{A2}$$

Here $f = e^{iq_x a_0/\sqrt{3}} + 2e^{-iq_x a_0/\sqrt{3}} \cos(q_y a_0/2)$, $a_0 = 2.46$ Å is the in-plane lattice parameter and $\mathbf{q}$ is the momentum. $\Delta_{12} = \alpha n_{p,12}$ is the interlayer potential difference between the bottom and middle layers, and $\Delta_{23} = \alpha n_{p,23}$ is the one between the middle and top layers, where $\alpha = e^2 c_0/(\varepsilon_0 \varepsilon)$, with $c_0 = 3.35$ Å as the interlayer distance, and ε is taken as 2.3 [63]. The carrier density parameters $n_{p,12}$ and $n_{p,23}$ satisfy

$$n_2 = n_{p,12} - n_{p,23},$$
$$n_3 = n_{\text{top}} + n_{p,23},$$
$$n_{\text{top}} + n_{\text{back}} = n_1 + n_2 + n_3,$$

where n_1 is the excess density of electrons on the closest layer to the back gate, and n_2 (n_3) is the excess density on the second (third) layer. n_{top} and n_{back} are the top and back gates induced electronic densities respectively.

In the Hamiltonian Eqs. (A1) and (A2), the parameters Δ_{12} and Δ_{23} are related to the carrier densities n_1, n_2, and n_3. On the other hand, the individual carrier densities are related to the eigenfunction of the Hamiltonian Eqs. (A1) and (A2) through [37,38],

$$n_l = \frac{1}{2\pi^2} \sum_i \int d^2\mathbf{q} \left(F(\epsilon_{i,\mathbf{q}}) - \frac{1}{2} \right) (|c_{A_l}|^2 + |c_{B_l}|^2) \tag{A3}$$

where $F(\epsilon) = (1 + e^{\frac{\epsilon-\mu}{K_B T}})^{-1}$ is the Fermi-Dirac distribution, i represents the different bands, and c_{A_l} and c_{B_l} (l = 1, 2, and 3, corresponding to the different layers) are the projections of the total electronic eigenfunction on the sublattices A_l and B_l. Therefore, the above equations are calculated self-consistently, following previous studies [37,38], with values of the coupling parameters shown in Table I.

2. Kubo formula

After obtaining the band structures, the Kubo formula is employed for calculated optical conductivities $\sigma(\omega)$ of the ABA and ABC graphene, written as $\sigma(\omega) = \sigma_{\text{D}}(\omega) + \sigma_{\text{IB}}(\omega)$. The intraband $[\sigma_{\text{D}}(\omega)]$ and interband $[\sigma_{\text{IB}}(\omega)]$ contributions are obtained from

$$\sigma_{\text{D}}(\omega) = 2\frac{\sigma_0}{\pi^2} \sum_i \int d^2\mathbf{q} \left| \langle \mathbf{q}, i | \frac{\partial H}{\partial q_x} | \mathbf{q}, i \rangle \right|^2 \times \left[-\frac{\partial F(\epsilon_{\mathbf{q},i})}{\partial \epsilon} \right] \frac{i}{\hbar\omega + i\Gamma_D}, \tag{A4}$$

$$\sigma_{\text{IB}}(\omega) = 2\frac{\sigma_0}{\pi^2} \sum_{i,j\neq i} \int d^2\mathbf{q} \left| \langle \mathbf{q}, i | \frac{\partial H}{\partial q_x} | \mathbf{q}, j \rangle \right|^2 \times \left[-\frac{f(\epsilon_{\mathbf{q},i}) - F(\epsilon_{\mathbf{q},j})}{\epsilon_{\mathbf{q},i} - \epsilon_{\mathbf{q},j}} \right] \frac{i}{\hbar\omega + \epsilon_{\mathbf{q},i} - \epsilon_{\mathbf{q},j} + i\Gamma_{IB}}, \tag{A5}$$

where $\sigma_0 = e^2/4\hbar \approx 6.08 \times 10^{-5}$ Ω^{-1}, and Γ_{D} and Γ_{IB} are the electronic broadening parameters for the two terms separately. In our calculations, the temperature is taken as T = 10 K. Temperature would have little influence on the imaginary parts of the optical conductivities and therefore the observation of plasmonic bandgap, as shown in Figs. 5(a) and 5(b). Moreover, as demonstrated in Fig. 2, the plasmonic bandgap occurs between the first band at K point and the second band at M point. Therefore, in Fig. 5(c) below, we show the calculated frequencies for the corresponding two points. Although a slight shift of the frequencies with temperature due to the Fermi-Dirac distributions, the plasmonic bandgap width is robust, and bandgap within 1275 and 1290 cm^{-1} is always expected for the various temperatures. On the other hand, concerning real parts of optical conductivities, which are relevant to plasmon damping, their quantitative characterizations require further experiments.

Noticeably, phonon-related conductivity effect [64,65] is not considered here, as it occurs at higher frequency (1585 cm^{-1}) and the peak is very narrow (2.5 cm^{-1}). Its influence on χ is negligible for the frequency range between 600 and 1300 cm^{-1} considered in the main text.

3. Optical conductivities at different doping levels

The conductivities of the ABA and ABC graphene are calculated at different backside-doped levels, as shown in Fig. 6. With the increase of doping, the transition peak at around $\omega = 2890$ cm^{-1} (close to γ_1, which is at 3035 cm^{-1}) of the ABC graphene at zero doping splits into two peaks P1 and P2, and the energy difference between these two peaks

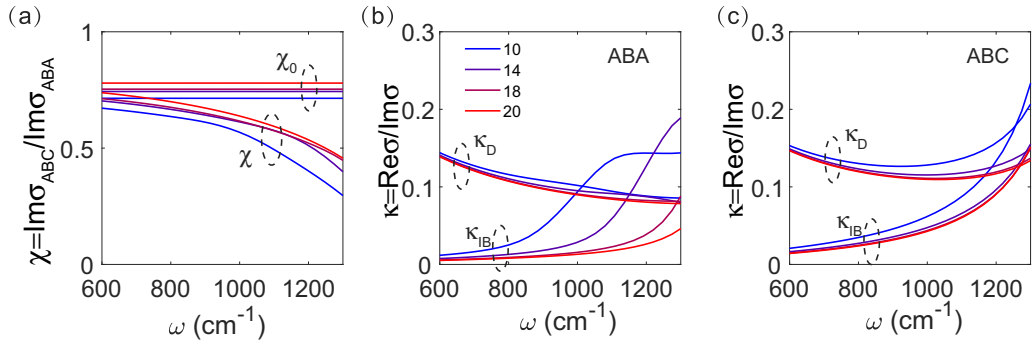

FIG. 7. (a) Calculated ratio of Imσ between the ABC and ABA graphene for different doping levels. χ_0 corresponds to the case where only the intraband terms are considered. [(b),(c)] Frequency-dependent damping factors for the ABA (b) and ABC (c) graphene. κ_D and κ_{IB} are the contributions from the intraband and interband terms, respectively. Here, electronic broadening parameters are assumed as $\Gamma_{IB} = \Gamma_D = 10$ meV.

increases with doping level. This phenomena corresponds to the opening of electronic bandgap [35].

Furthermore, Fig. 7 presents the dependence of ratio parameter $\chi = \mathrm{Im}\sigma_{ABC}/\mathrm{Im}\sigma_{ABA}$ and damping factors with light frequency ranging from 600 to 1300 cm^{-1} for varied carrier densities from 10 to 20 $\times$ 10^{12} cm^{-2}. Consistence with the main text, χ decreases with the increase of frequency for all the investigated doping levels. Moreover, the interband transition related damping factors κ_{IB} stay at the same level of κ_D for all cases, if assuming same electronic broadening parameters in the Kubo formula.

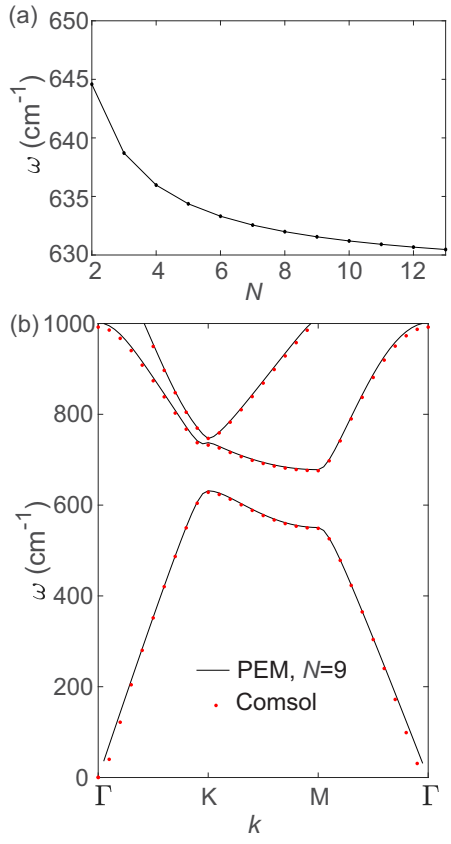

FIG. 8. Comparison between PEM and Comsol. (a) Calculated N-dependent eigenfrequency of the first plasmonic band at the K point for the GPC. (b) Comparison between the PEM and Comsol, where $N = 9$ is taken in the PEM. The lattice constant of the GPC is taken as $a = 150$ nm.

APPENDIX B: CALCULATIONS OF THE BULK PLASMONIC BAND STRUCTURES

1. Description of the plane-wave expansion method (PEM)

PEM is widely employed for band structure calculations of graphene plasmonic crystals [6,9,11]. It starts from the equation of the quasistatic in-plane potential $\varphi(\mathbf{r})$ for a periodically varying conductivity $\sigma(\mathbf{r})$,

$$\varphi(\mathbf{r}) = \frac{i}{4\pi\varepsilon_0\varepsilon_r\omega}\int d^2\mathbf{r}'\frac{\nabla\cdot[\sigma(\mathbf{r}')\nabla\varphi(\mathbf{r}')]}{|\mathbf{r}'-\mathbf{r}|}, \tag{B1}$$

where ε_r is the efficient dielectric constant of the environment, and ω is the angular frequency of light.

The periodic conductivity can be written in terms of reciprocal lattice vectors $\mathbf{G}_m$,

$$\sigma(\mathbf{r}) = \sum_m \sigma_{\mathbf{G_m}} e^{i\mathbf{G_m}\cdot\mathbf{r}}. \tag{B2}$$

Meanwhile, the in-plane potential $\varphi(\mathbf{r})$ has the Bloch form,

$$\varphi(\mathbf{r}) = \sum_m p_m e^{i(\mathbf{G}_m+\mathbf{k})\cdot\mathbf{r}}. \tag{B3}$$

Equation (B1) then becomes an eigenproblem. In $\mathbf{k}$ space,

$$HC = AC, \tag{B4}$$

where the elements of H are

$$H_{m,n} = \frac{(\mathbf{G}_m+\mathbf{k})\cdot(\mathbf{G}_n+\mathbf{k})}{\sqrt{|\mathbf{G}_m+\mathbf{k}||\mathbf{G}_n+\mathbf{k}|}}\sigma_{\mathbf{G_m}-\mathbf{G_n}}. \tag{B5}$$

The eigenvector C has elements $C_m = p_m\sqrt{|\mathbf{G}_m+\mathbf{k}|}$, and the eigenvalue is $A = 2i\varepsilon_0\varepsilon_r\omega a$. Therefore, ε_r and a enters the eigenvalue problem through $\varepsilon_r a$, and ε_r is assumed as 1 in this paper. For the moiré superlattices where the domain walls are neglected, $\sigma_{\mathbf{G_m}}$ at a reciprocal lattice vector $\mathbf{G}_m = l_1\mathbf{b}_1 + l_2\mathbf{b}_2$ can be obtained analytically, which is expressed as

$$\frac{1}{2}(\sigma_1+\sigma_2), \quad \text{if } l_1 = 0, l_2 = 0,$$

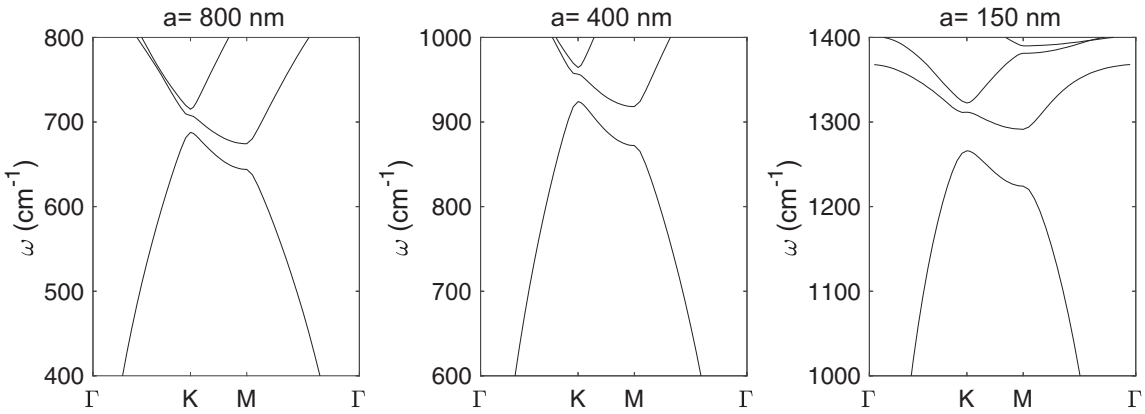

FIG. 9. Opening of plasmonic bandgap with the decrease of moiré period a, which occurs at high frequency when χ is low.

$$
\begin{cases}
(\sigma_1-\sigma_2)\dfrac{i}{2\pi l_2}, & \text{if } l_1=0, l_2\neq 0,\\
-(\sigma_1-\sigma_2)\dfrac{i}{2\pi l_1}, & \text{if } l_1\neq 0, l_2=0,\\
0, & \text{if } l_1\neq 0, l_2\neq 0, l_1+l_2\neq 0,\\
(\sigma_1-\sigma_2)\dfrac{i}{2\pi l_1}, & \text{if } l_1\neq 0, l_2\neq 0, l_1+l_2=0.
\end{cases}
$$

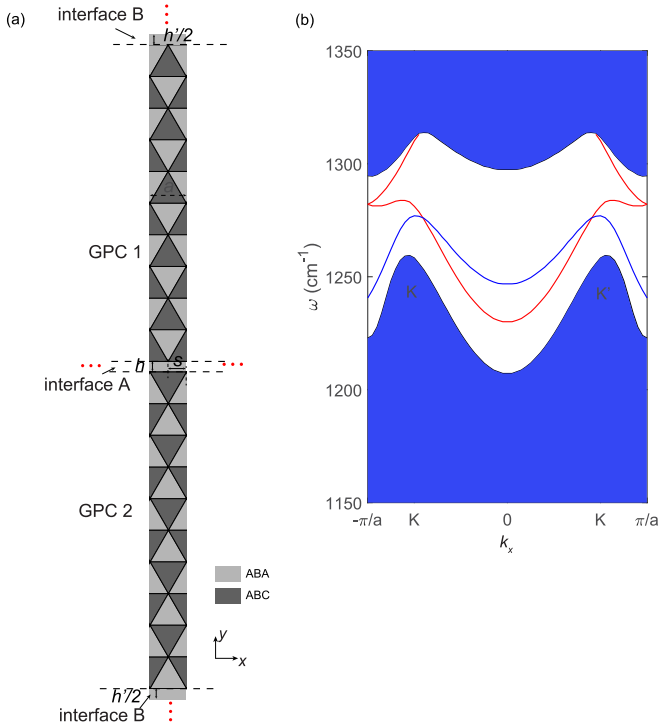

FIG. 10. Calculation details of plasmonic edge states. (a) Schematic of the structures of the unit cell used in the calculation, which are periodic in both x and y directions, with the interfaces A (width of h) and B (width of h') separating regions GPC1 and GPC2. The two GPCs are shifted in x direction by s. (b) Dispersions of edge states for the two interfaces, where the red and blue curves are the edge modes for interfaces A and B, respectively. Here, $h = h' = a/(2\sqrt{3})$ and $s = 0.5a$.

The frequency dependence of $\sigma_{\mathbf{G_m}}$ is considered in calculating Figs. 2, 3, and 4 of the main text. We adopted a numerical convergence method, which was coded in Matlab to solve the frequency dependent Eqs. (11) and (12). Each plasmonic band is calculated separately. For calculating each plasmonic band, there are many loops in the calculations. For the first loop $j = 1$, we set a very high hypothetical input value of ω expressed as $\omega_{\text{in},1}$, with which one can get the values of $\sigma_{\mathbf{G_m}-\mathbf{G_n}}$ from the above analytical expressions. This $\omega_{\text{in},1}$ in only works for calculating $\sigma_{\mathbf{G_m}-\mathbf{G_n}}$. Then by solving Eqs. (11) and (12), one can get a calculated output value of ω expressed as $\omega_{\text{out},1}$. Then for the second loop $j = 2$, we set $\omega_{\text{in},2}$ as $\omega_{\text{in},2} = \omega_{\text{out},1}$, and repeat the above procedure again. After j loops, the values of ω_{out}, j and ω_{in}, j would be very close. The convergence condition in our calculation is $|\omega_{\text{out}}, j\text{-}\omega_{\text{in}}, j| < 0.1\ \text{cm}^{-1}$, which is precise enough, and typically converges very efficiently (around 10 to 20 loops).

On the other hand, in the PEM, the reciprocal lattice vectors are defined as $\mathbf{G}_m = l_1\mathbf{b}_1 + l_2\mathbf{b}_2$, where the integers l_1 and l_2 take values of $\{-N, -N+1, ..., -1, 0, 1, ..., N-1, N\}$. Here, the positive integer N determines calculation accuracy. Convergence of the calculated eigenfrequency with N is tested and shown in Fig. 8(a). The result converges fast with the increase of N. Moreover, Fig. 8(b) compares the calculated plasmonic band structures from PEM with those from Comsol. Only for Fig. 8 here, optical conductivities of the ABA and ABC graphene are taken as $2i\sigma_0$ and $i\sigma_0$ respectively, which are for the comparison and not related to the actual case. For a value of $N = 9$, PEM generates consistent results with Comsol, while saves huge a lot of time. Therefore, PEM is adopted in the calculations of plasmonic dispersions of the 2D and edge modes in the main text, and $N = 9$ is employed for calculating the 2D plasmon modes.

2. Opening of plasmonic bandgap

The opening of plasmonic bandgap is determined by the parameter χ as shown in Fig. 2. To further elaborate on this, we show in Fig. 9 the plasmonic band structures for various values of the moiré period a, which determines the frequency of plasmonic bandgap. For higher values of a, the first and second plasmonic bands split at lower frequencies, and moreover their separation becomes smaller. The latter stems from

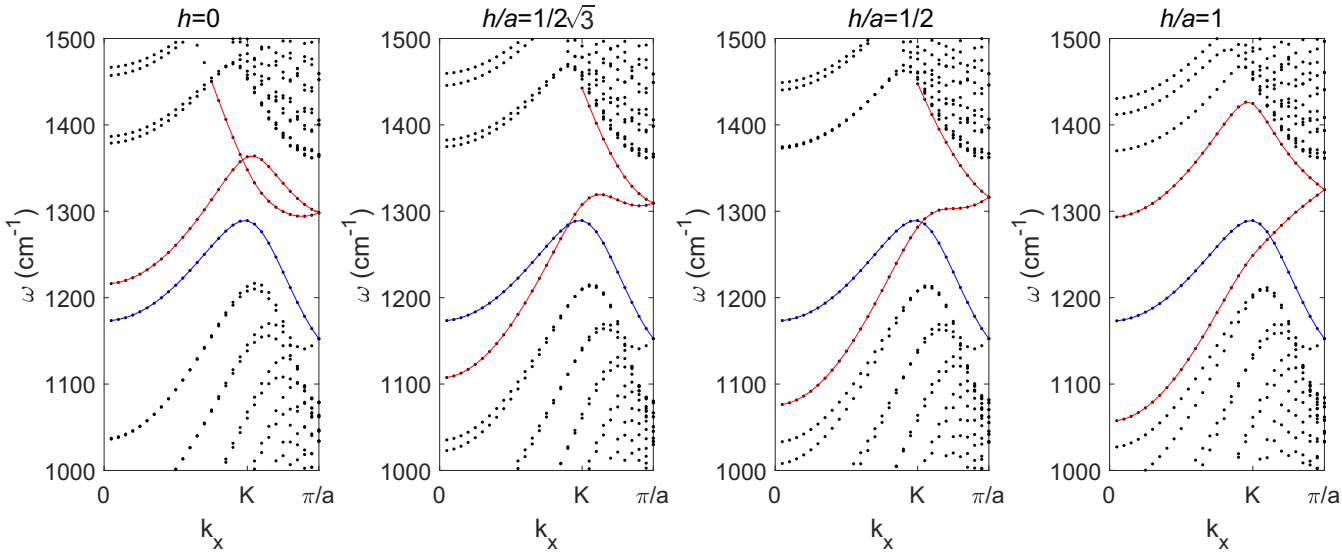

FIG. 11. Influence of the interface width h on the edge state dispersions. The red and blue curves are the edge modes for the interfaces A and B, respectively. Here, $s = 0.5a$. For simplicity, frequency-independent values of conductivity for the ABA and ABC graphene are taken as the ones at $\omega = 1270\ \mathrm{cm}^{-1}$.

the higher values of χ at lower frequencies. For example, χ is around 0.7 at 700 cm^{-1}, 0.65 at 900 cm^{-1} and 0.5 at 1200 cm^{-1}. Therefore, a large separation between the first and second bands and therefore the existence of a direct plasmonic bandgap is expected at high frequency when χ is low.

APPENDIX C: CALCULATIONS OF THE PLASMONIC EDGE STATES

For the numerical calculation of edge states, periodic conditions in both x and y directions are employed, and Fig. 10(a) presents the structures of the unit cell. There exists two interfaces with widths h (interface A) and h' (interface B) separating the two GPCs. Edge states of the interface A is presented in the main text. In the calculation, finite height of $5\sqrt{3}a$ for the two GPCs are used, which is large enough to ensure the calculation accuracy of edge states. Moreover, in the PEM, different values of N are necessary for the x (N_x) and y (N_y) directions [11]. In our calculations, $N_x = 7$ and N_y is proportionally scaled according to spatial sizes of the unit cell in these two directions. Figure 10(b) presents the calculated dispersions for the edge states of the two interfaces, where the red and blue curves correspond to the edge modes for the interfaces A and B, respectively.

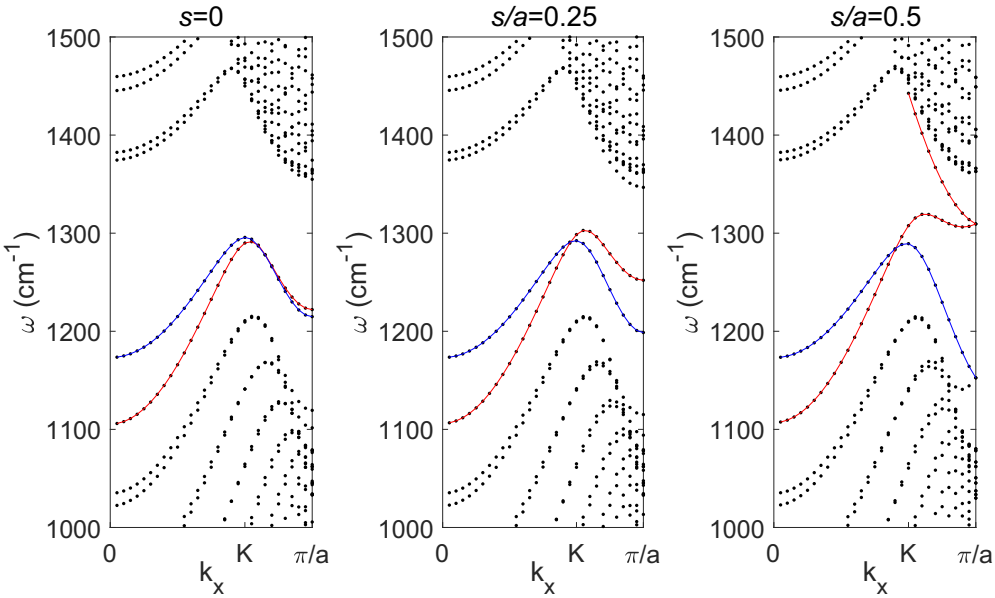

FIG. 12. Influence of the shift parameter s on the edge state dispersions. The red and blue curves are the edge modes for the interfaces A and B, respectively. Here, $h = h' = a/(2\sqrt{3})$. For simplicity, frequency-independent values of conductivity for the ABA and ABC graphene are taken as the ones at $\omega = 1270\ \mathrm{cm}^{-1}$.

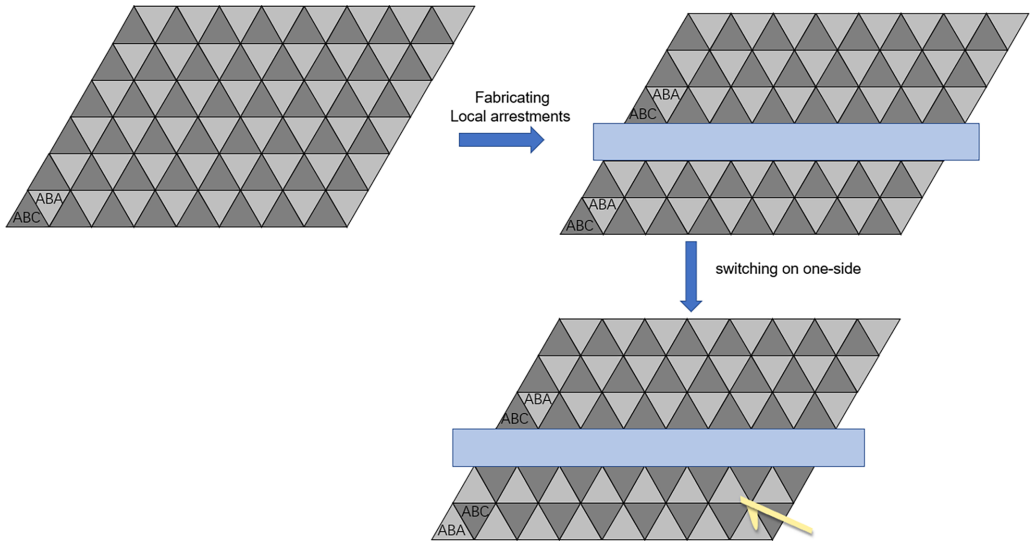

FIG. 13. A proposal for fabricating the interface structures, including twisting, local arrestments fabrication, and switching.

Furthermore, evolutions of the edge states at the interface A with varied geometric parameters h and s are investigated, as shown in Figs. 11 and 12 (red curves). Here, for simplicity and without loss of the trends, frequency-independent values of conductivity for the ABA and ABC graphene are taken as the ones at $\omega = 1270\ \mathrm{cm}^{-1}$. Existing frequency range of the edge states varies with these two parameters. Nonetheless, in practice, careful design of the geometric parameters can be done via local engineering of the stacking domains [26,31,53] to maximize the existing frequency range.

APPENDIX D: POSSIBLE EXPERIMENTAL REALIZATIONS

In practice, the interface structures can be fabricated by combining twisting, local modifications and switching. In previous studies [26], the stacking domains can be switched by local load imposed from AFM tip and the switching can propagate spontaneously in a domino-like fashion. Moreover, local arrestments/confinements like wrinkles can completely block the propagation of switching, resulting in two regions with heterogenous domains with diverse patterns. Accordingly, we propose a possible approach for fabricating the interface structures, as illustrated in Fig. 13. Firstly, the periodic domains are prepared by twisting between monolayer and bilayer graphene. Secondly, local arrestments are created by various kinds of approaches like AFM writing [66] or ion beam modifications [67]. Finally, stacking orders on one side is switched by local load, resulting in an interface separating domains with opposite valley Chern numbers. Furthermore, the rapid advances in understanding and manipulations of

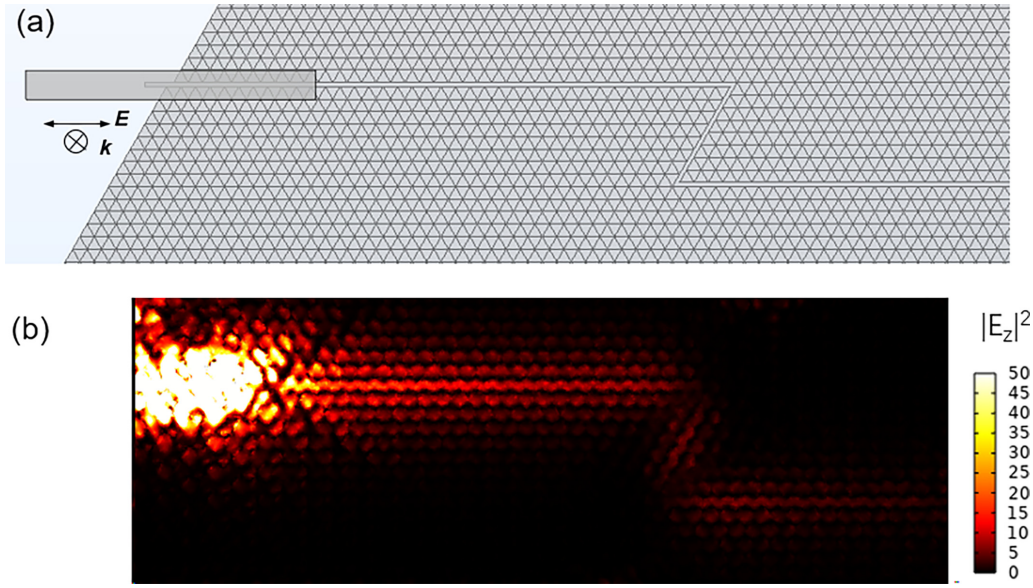

FIG. 14. The edge states can be excited by near-field of an resonant antenna under far-field illuminations. Here, a gold rod with length, width and height of 3, 0.3, and 0.1 μm is utilized. The light frequency is at 1270 cm^{-1}.

moiré superlattices would benefit precise fabrications of the interface structures.

Excitations of the edge states can be realized experimentally by far-field illuminations on a metallic antenna nearby, as demonstrated numerically in Fig. 14. Moreover, scattering-type scanning near-field microscopy can be employed for detecting the edge states. Similar configurations have been employed for excitation and detection of propagating plasmons in graphene plasmonic crystals [7,8].

[1] F. H. Koppens, D. E. Chang, and F. J. García de Abajo, Graphene plasmonics: A platform for strong light–matter interactions, Nano Lett. **11**, 3370 (2011).

[2] A. Woessner, M. B. Lundeberg, Y. Gao, A. Principi, P. Alonso-González, M. Carrega, K. Watanabe, T. Taniguchi, G. Vignale, M. Polini *et al.*, Highly confined low-loss plasmons in graphene–boron nitride heterostructures, Nat. Mater. **14**, 421 (2015).

[3] G. Ni, d. A. McLeod, Z. Sun, L. Wang, L. Xiong, K. Post, S. Sunku, B.-Y. Jiang, J. Hone, C. R. Dean *et al.*, Fundamental limits to graphene plasmonics, Nature (London) **557**, 530 (2018).

[4] A. Vakil and N. Engheta, Transformation optics using graphene, Science **332**, 1291 (2011).

[5] D. Rodrigo, O. Limaj, D. Janner, D. Etezadi, F. J. García de Abajo, V. Pruneri, and H. Altug, Mid-infrared plasmonic biosensing with graphene, Science **349**, 165 (2015).

[6] I. Silveiro, A. Manjavacas, S. Thongrattanasiri, and F. G. De Abajo, Plasmonic energy transfer in periodically doped graphene, New J. Phys. **15**, 033042 (2013).

[7] L. Xiong, C. Forsythe, M. Jung, A. McLeod, S. Sunku, Y. Shao, G. Ni, A. Sternbach, S. Liu, J. Edgar *et al.*, Photonic crystal for graphene plasmons, Nat. Commun. **10**, 4780 (2019).

[8] L. Xiong, Y. Li, M. Jung, C. Forsythe, S. Zhang, A. S. McLeod, Y. Dong, S. Liu, F. L. Ruta, and C. Li *et al.*, Programmable bloch polaritons in graphene, Sci. Adv. **7**, eabe8087 (2021).

[9] D. Jin, T. Christensen, M. Soljačić, N. X. Fang, L. Lu, and X. Zhang, Infrared topological plasmons in graphene, Phys. Rev. Lett. **118**, 245301 (2017).

[10] D. Pan, R. Yu, H. Xu, and F. J. García de Abajo, Topologically protected Dirac plasmons in a graphene superlattice, Nat. Commun. **8**, 1243 (2017).

[11] M. Jung, Z. Fan, and G. Shvets, Midinfrared plasmonic valleytronics in metagate-tuned graphene, Phys. Rev. Lett. **121**, 086807 (2018).

[12] J. Lu, C. Qiu, M. Ke, and Z. Liu, Valley vortex states in sonic crystals, Phys. Rev. Lett. **116**, 093901 (2016).

[13] T. Ma and G. Shvets, All-Si valley-Hall photonic topological insulator, New J. Phys. **18**, 025012 (2016).

[14] J.-W. Liu, F.-L. Shi, X.-T. He, G.-J. Tang, W.-J. Chen, X.-D. Chen, and J.-W. Dong, Valley photonic crystals, Adv. Phys.: X **6**, 1905546 (2021).

[15] E. Suárez Morell, J. Correa, P. Vargas, M. Pacheco, and Z. Barticevic, Flat bands in slightly twisted bilayer graphene: Tight-binding calculations, Phys. Rev. B **82**, 121407(R) (2010).

[16] Y. Cao, V. Fatemi, A. Demir, S. Fang, S. L. Tomarken, J. Y. Luo, J. D. Sanchez-Yamagishi, K. Watanabe, T. Taniguchi, E. Kaxiras *et al.*, Correlated insulator behaviour at half-filling in magic-angle graphene superlattices, Nature (London) **556**, 80 (2018).

[17] Y. Cao, V. Fatemi, S. Fang, K. Watanabe, T. Taniguchi, E. Kaxiras, and P. Jarillo-Herrero, Unconventional superconductivity in magic-angle graphene superlattices, Nature (London) **556**, 43 (2018).

[18] Y. Shimazaki, I. Schwartz, K. Watanabe, T. Taniguchi, and M. Kroner, A. Imamoğlu, Strongly correlated electrons and hybrid excitons in a moiré heterostructure, Nature (London) **580**, 472 (2020).

[19] C. Jin, E. C. Regan, A. Yan, M. IqbalBakti Utama, D. Wang, S. Zhao, Y. Qin, S. Yang, Z. Zheng, S. Shi *et al.*, Observation of moiré excitons in WSe_2/WS_2 heterostructure superlattices, Nature (London) **567**, 76 (2019).

[20] Z. Hao, A. Zimmerman, P. Ledwith, E. Khalaf, D. H. Najafabadi, K. Watanabe, T. Taniguchi, A. Vishwanath, and P. Kim, Electric field–tunable superconductivity in alternating-twist magic-angle trilayer graphene, Science **371**, 1133 (2021).

[21] L. Du, M. R. Molas, Z. Huang, G. Zhang, F. Wang, and Z. Sun, Moiré photonics and optoelectronics, Science **379**, eadg0014 (2023).

[22] H. Yoo, R. Engelke, S. Carr, S. Fang, K. Zhang, P. Cazeaux, S. H. Sung, R. Hovden, A. W. Tsen, T. Taniguchi *et al.*, Atomic and electronic reconstruction at the van der Waals interface in twisted bilayer graphene, Nat. Mater. **18**, 448 (2019).

[23] A. Weston, Y. Zou, V. Enaldiev, A. Summerfield, N. Clark, V. Zólyomi, A. Graham, C. Yelgel, S. Magorrian, M. Zhou *et al.*, Atomic reconstruction in twisted bilayers of transition metal dichalcogenides, Nat. Nanotechnol. **15**, 592 (2020).

[24] D. Halbertal, S. Turkel, C. J. Ciccarino, J. B. Hauck, N. Finney, V. Hsieh, K. Watanabe, T. Taniguchi, J. Hone, C. Dean *et al.*, Unconventional non-local relaxation dynamics in a twisted trilayer graphene moiré superlattice, Nat. Commun. **13**, 7587 (2022).

[25] S. Sunku, G. Ni, B.-Y. Jiang, H. Yoo, A. Sternbach, A. McLeod, T. Stauber, L. Xiong, T. Taniguchi, K. Watanabe *et al.*, Photonic crystals for nano-light in moiré graphene superlattices, Science **362**, 1153 (2018).

[26] S. Zhang, Q. Xu, Y. Hou, A. Song, Y. Ma, L. Gao, M. Zhu, T. Ma, L. Liu, X.-Q. Feng *et al.*, Domino-like stacking order switching in twisted monolayer–multilayer graphene, Nat. Mater. **21**, 621 (2022).

[27] L. Brey, T. Stauber, T. Slipchenko, L. Martín-Moreno, Plasmonic Dirac cone in twisted bilayer graphene, Phys. Rev. Lett. **125**, 256804 (2020).

[28] D. Halbertal, N. R. Finney, S. S. Sunku, A. Kerelsky, C. Rubio-Verdú, S. Shabani, L. Xian, S. Carr, S. Chen, C. Zhang *et al.*, Moiré metrology of energy landscapes in van der Waals heterostructures, Nat. Commun. **12**, 242 (2021).

[29] M. R. Rosenberger, H.-J. Chuang, M. Phillips, V. P. Oleshko, K. M. McCreary, S. V. Sivaram, C. S. Hellberg, and B. T. Jonker, Twist angle-dependent atomic reconstruction and moiré

patterns in transition metal dichalcogenide heterostructures, ACS Nano **14**, 4550 (2020).

[30] S. Moore, C. Ciccarino, D. Halbertal, L. McGilly, N. Finney, K. Yao, Y. Shao, G. Ni, A. Sternbach, E. Telford *et al.*, Nanoscale lattice dynamics in hexagonal boron nitride moiré superlattices, Nat. Commun. **12**, 5741 (2021).

[31] H. Li, M. I. B. Utama, S. Wang, W. Zhao, S. Zhao, X. Xiao, Y. Jiang, L. Jiang, T. Taniguchi, K. Watanabe *et al.*, Global control of stacking-order phase transition by doping and electric field in few-layer graphene, Nano Lett. **20**, 3106 (2020).

[32] K. F. Mak, J. Shan, and T. F. Heinz, Electronic structure of few-layer graphene: experimental demonstration of strong dependence on stacking sequence, Phys. Rev. Lett. **104**, 176404 (2010).

[33] W. Bao, L. Jing, J. Velasco Jr, Y. Lee, G. Liu, D. Tran, B. Standley, M. Aykol, S. Cronin, D. Smirnov *et al.*, Stacking-dependent band gap and quantum transport in trilayer graphene, Nat. Phys. **7**, 948 (2011).

[34] A. F. Morpurgo, The ABC of 2D materials, Nat. Phys. **11**, 625 (2015).

[35] C. H. Lui, Z. Li, K. F. Mak, E. Cappelluti, and T. F. Heinz, Observation of an electrically tunable band gap in trilayer graphene, Nat. Phys. **7**, 944 (2011).

[36] Y. Luan, J. Qian, M. Kim, K.-M. Ho, Y. Shi, Y. Li, C.-Z. Wang, M. C. Tringides, and Z. Fei, Imaging stacking-dependent surface plasmon polaritons in trilayer graphene, Phys. Rev. Applied **18**, 024052 (2022).

[37] A. A. Avetisyan, B. Partoens, and F. M. Peeters, Electric field tuning of the band gap in graphene multilayers, Phys. Rev. B **79**, 035421 (2009).

[38] N. Ubrig, P. Blake, D. Van Der Marel, and A. Kuzmenko, Infrared spectroscopy of hole-doped ABA-stacked trilayer graphene, Europhys. Lett. **100**, 58003 (2012).

[39] H. Mei, W. Xu, C. Wang, H. Yuan, C. Zhang, L. Ding, J. Zhang, C. Deng, Y. Wang, and F. M. Peeters, Terahertz magneto-optical properties of bi- and tri-layer graphene, J. Phys.: Condens. Matter **30**, 175701 (2018).

[40] M. S. Choi, A. Nipane, B. S. Kim, M. E. Ziffer, I. Datta, A. Borah, Y. Jung, B. Kim, D. Rhodes, A. Jindal *et al.*, High carrier mobility in graphene doped using a monolayer of tungsten oxyselenide, Nat. Electron. **4**, 731 (2021).

[41] X.-T. He, E.-T. Liang, J.-J. Yuan, H.-Y. Qiu, X.-D. Chen, F.-L. Zhao, and J.-W. Dong, A silicon-on-insulator slab for topological valley transport, Nat. Commun. **10**, 872 (2019).

[42] J.-L. Liu, W.-M. Ye, and S. Zhang, Pseudospin-induced chirality with staggered optical graphene, Light: Sci. Appl. **5**, e16094 (2016).

[43] X.-D. Chen, F.-L. Zhao, M. Chen, and J.-W. Dong, Valley-contrasting physics in all-dielectric photonic crystals: Orbital angular momentum and topological propagation, Phys. Rev. B **96**, 020202(R) (2017).

[44] S. Chakraborty, O. Marshall, T. Folland, Y.-J. Kim, A. Grigorenko, and K. Novoselov, Gain modulation by graphene plasmons in aperiodic lattice lasers, Science **351**, 246 (2016).

[45] D. Svintsov, Z. Devizorova, T. Otsuji, and V. Ryzhii, Plasmons in tunnel-coupled graphene layers: Backward waves with quantum cascade gain, Phys. Rev. B **94**, 115301 (2016).

[46] J. W. You, Z. Lan, and N. C. Panoiu, Four-wave mixing of topological edge plasmons in graphene metasurfaces, Sci. Adv. **6**, eaaz3910 (2020).

[47] F. Guan, X. Guo, S. Zhang, K. Zeng, Y. Hu, C. Wu, S. Zhou, Y. Xiang, X. Yang, and Q. Dai, and S. Zhang, Compensating losses in polariton propagation with synthesized complex frequency excitation, Nat. Mater. **23**, 506 (2024).

[48] N. P. Kazmierczak, M. Van Winkle, C. Ophus, K. C. Bustillo, S. Carr, H. G. Brown, J. Ciston, T. Taniguchi, K. Watanabe, and D. K. Bediako, Strain fields in twisted bilayer graphene, Nat. Mater. **20**, 956 (2021).

[49] C. N. Lau, M. W. Bockrath, K. F. Mak, and F. Zhang, Reproducibility in the fabrication and physics of moiré materials, Nature (London) **602**, 41 (2022).

[50] M. Kapfer, B. S. Jessen, M. E. Eisele, M. Fu, D. R. Danielsen, T. P. Darlington, S. L. Moore, N. R. Finney, A. Marchese, V. Hsieh *et al.*, Programming twist angle and strain profiles in 2D materials, Science **381**, 677 (2023).

[51] A. Karalis, E. Lidorikis, M. Ibanescu, J. Joannopoulos, M. Soljačić, Surface-plasmon-assisted guiding of broadband slow and subwavelength light in air, Phys. Rev. Lett. **95**, 063901 (2005).

[52] V. Hsieh, D. Halbertal, N. R. Finney, Z. Zhu, E. Gerber, M. Pizzochero, E. Kucukbenli, G. R. Schleder, M. Angeli, K. Watanabe *et al.*, Domain-dependent surface adhesion in twisted few-layer graphene: Platform for moiré-assisted chemistry, Nano Lett. **23**, 3137 (2023).

[53] M. Yankowitz, J. I.-J. Wang, A. G. Birdwell, Y.-A. Chen, K. Watanabe, T. Taniguchi, P. Jacquod, P. San-Jose, P. Jarillo-Herrero, and B. J. LeRoy, Electric field control of soliton motion and stacking in trilayer graphene, Nat. Mater. **13**, 786 (2014).

[54] B.-Y. Jiang, G.-X. Ni, Z. Addison, J. K. Shi, X. Liu, S. Y. F. Zhao, P. Kim, E. J. Mele, D. N. Basov, and M. M. Fogler, Plasmon reflections by topological electronic boundaries in bilayer graphene, Nano Lett. **17**, 7080 (2017).

[55] M. Vizner Stern, Y. Waschitz, W. Cao, I. Nevo, K. Watanabe, T. Taniguchi, E. Sela, M. Urbakh, O. Hod, and M. Ben Shalom, Interfacial ferroelectricity by van der Waals sliding, Science **372**, 1462 (2021).

[56] K. Yasuda, X. Wang, K. Watanabe, T. Taniguchi, and P. Jarillo-Herrero, Stacking-engineered ferroelectricity in bilayer boron nitride, Science **372**, 1458 (2021).

[57] Y. Zhang, R. Polski, C. Lewandowski, A. Thomson, Y. Peng, Y. Choi, H. Kim, K. Watanabe, T. Taniguchi, J. Alicea *et al.*, Promotion of superconductivity in magic-angle graphene multilayers, Science **377**, 1538 (2022).

[58] Y. Zeng, Z. Xia, R. Dery, K. Watanabe, T. Taniguchi, J. Shan, and K. F. Mak, Exciton density waves in Coulomb-coupled dual moiré lattices, Nat. Mater. **22**, 175 (2023).

[59] X. Cai and W. Gao, Moiré synergy: An emerging game changer by Moiré of Moiré, arXiv:2303.01858.

[60] S. Guddala, F. Komissarenko, S. Kiriushechkina, A. Vakulenko, M. Li, V. Menon, A. Alù, and A. Khanikaev, Topological phonon-polariton funneling in midinfrared metasurfaces, Science **374**, 225 (2021).

[61] W. Liu, Z. Ji, Y. Wang, G. Modi, M. Hwang, B. Zheng, V. J. Sorger, A. Pan, and R. Agarwal, Generation of helical topological exciton-polaritons, Science **370**, 600 (2020).

[62] N. C. Hesp, I. Torre, D. Rodan-Legrain, P. Novelli, Y. Cao, S. Carr, S. Fang, P. Stepanov, D. Barcons-Ruiz, H. Herzig Sheinfux *et al.*, Observation of interband collective excitations in twisted bilayer graphene, Nat. Phys. **17**, 1162 (2021).

[63] A. Avetisyan, B. Partoens, and F. Peeters, Electric-field control of the band gap and fermi energy in graphene multilayers by top and back gates, Phys. Rev. B **80**, 195401 (2009).

[64] J. Qian, Y. Luan, M. Kim, K.-M. Ho, Y. Shi, C.-Z. Wang, Y. Li, and Z. Fei, Nonequilibrium phonon tuning and mapping in few-layer graphene with infrared nanoscopy, Phys. Rev. B **103**, L201407 (2021).

[65] P. Shen, X. Zhou, J. Chen, A. Deng, B. Lyu, Z. Zhang, S. Lou, S. Ma, B. Wei, and Z. Shi, Quick identification of ABC trilayer graphene at nanoscale resolution via a near-field optical route, Mater. Futures **2**, 015301 (2023).

[66] H. Li, Z. Ying, B. Lyu, A. Deng, L. Wang, T. Taniguchi, K. Watanabe, and Z. Shi, Electrode-free anodic oxidation nanolithography of low-dimensional materials, Nano Lett. **18**, 8011 (2018).

[67] W. Luo, W. Cai, W. Wu, Y. Xiang, M. Ren, X. Zhang, and J. Xu, Tailorable reflection of surface plasmons in defect engineered graphene, 2D Mater. **3**, 045001 (2016).